Effective Date: 12/11/2023
Expiration Date: 12/11/2028

XRISM/ Resolve
CMO
12/11/2023
RELEASED

INSTRUMENT CALIBRATION REPORT

RESOLVE DEWAR GATE VALVE TRANSMISSION

RESOLVE-SCI-RPT-0159

REVISION -

XRISM-RESOLVE-CALDB-GATEVALVE-213

X-ray Imaging and Spectroscopy Mission (XRISM) Project

NASA/GSFC Code 461

.

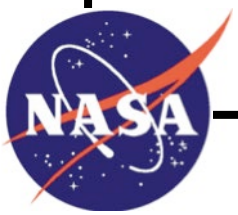

National Aeronautics and
Space Administration

Goddard Space Flight Center
Greenbelt, Maryland

Check https://ipdtdms.gsfc.nasa.gov
to verify that this is the correct version prior to use

RESOLVE DEWAR GATE VALVE TRANSMISSION
Signature/Approval Page

Prepared by:

Takuya Midooka (U. of Tokyo), Masahiro Tsujimoto (ISAS/JAXA), Shunji Kitamoto (Rikkyo U.), Megan E. Eckart (LLNL), Tahir Yaqoob (GSFC/NASA), and the Resolve Instrument Team

Reviewers/Approvers:

Megan Eckart
Maurice Leutenegger
Michael Lowenstein
Tahir Yaqoob

Approved by:

Megan Eckart

***** Electronic signatures are available on-line at: https://ipdtdms.gsfc.nasa.gov*****

Preface

This document is an XRISM Project signature-controlled document. Changes to this document require prior approval of the applicable Product Design Lead (PDL) or designee. Proposed changes shall be submitted in the Technical Data Management System (TDMS) via a Signature Control Request (SCoRe) along with supportive material justifying the proposed change. Changes to this document will be made by complete revision.

All of the requirements in this document assume the use of the word "shall" unless otherwise stated.

Questions or comments concerning this document should be addressed to:
XRISM Configuration Management Office
Mail Stop: 461
Goddard Space Flight Center
Greenbelt, Maryland 20771

Change History Log

Revision	Effective Date	Description of Changes (Reference the SCoRe Approval Date)
-	12/11/2023	First version of report based on ground measurements. Includes effects of Resolve support structure geometry (no cross, a change from SXS), measurements and modeling of the transmission of the protective stainless steel mesh (measurements are new, compared to SXS), and transmission measurements and modeling of GV beryllium window, including measurements of non-uniforimty. Released per RESOLVE-SCoRe-0567.

NOTE to editors: The document name will be XRISM-CAL-RPT-XXXX, where XXXX is assigned by the TDMS system. The document will be cross-referenced in TDMS to the filename in the format XRISM-XXX-CALDB-FILEDESC-NN where XXX is the instrument or component (e.g. RESOLVE), FILEDESC refers to a specific calibration report (e.g., rmfparams) and NN the corresponding number assigned to that report by the SDC. For example, the calibration report addressing the Resolve LSF calibration may be assigned XRISM-RESOLVE-CALDB-RMFPARAMS-01, that addressing the Resolve gain calibration XRISM-RESOLVE-GAINPIX-CALDB-02, etc. (where the numbers are to be provided by the SDC).

These documents are updated as needed, e.g. when the relevant CalDB files, or the relevant calibration data analysis, is revised. The document version will be assigned by the TDMS system. The tracking tool should be used to record changes.

This document must include the CalDB file name, an explanation of how the data were collected and the analysis conducted and, if using standard Ftools, the software version number. All revisions are consolidated into the same document to maintain a full record of all changes.

Table of Contents

1 Introduction

1.1 Purpose

The Resolve Dewar gate valve (GV) will be opened in orbit during the commissioning phase after the initial spacecraft outgassing. Until then, the GV is part of the optical path for all observations. The GV CalDB file is used to make corrections for the energy and spatial dependence of the X-ray transmission of the two components of the GV aperture: the Be window and the protective stainless steel mesh.

1.2 Structure of this document

This document is structured as follows. First, we start with a brief description of the gate valve in Section 2, and describe differences between the gate valve geometry between the Astro-H Soft X-ray Spectrometer (SXS). In Section 3, we describe the ground calibration measurements of the X-ray transmission for (i) the energy dependence of the Be window (Section 3.1), (ii) that of the stainless steel mesh (Section 3.2), and (iii) spatial dependence of the Be window (Section 3.3). Each subsection consists of setup, results and modeling. Based on these measurements, we made the pre-launch release of the CalDB file in Section 4. Additional details of the ground-calibration results are given in [1] and [11].

1.3 Scientific Impact

In ASTRO-H SXS, all observations are affected by the presence of the GV along the optical path. Partly because the flight model was not calibrated before the launch, the uncertainty caused by the GV was a large contributor to the overall uncertainty in the effective area [4].

2 Dewar gate valve

2.1 Overview

The GV has two parts in the X-ray optical path when it is closed; (1) Be window and (2) stainless mesh for protecting the Be window. A picture of these components is shown in Figure 1, while their materials and dimensions are given in Table 1.

The GV is supplied by the Sumitomo Heavy Industries (SHI), which is the prime contractor of the Resolve Dewar. The Be window is manufactured by Brush Wellman Ltd., which is now a part of Materion Corp.

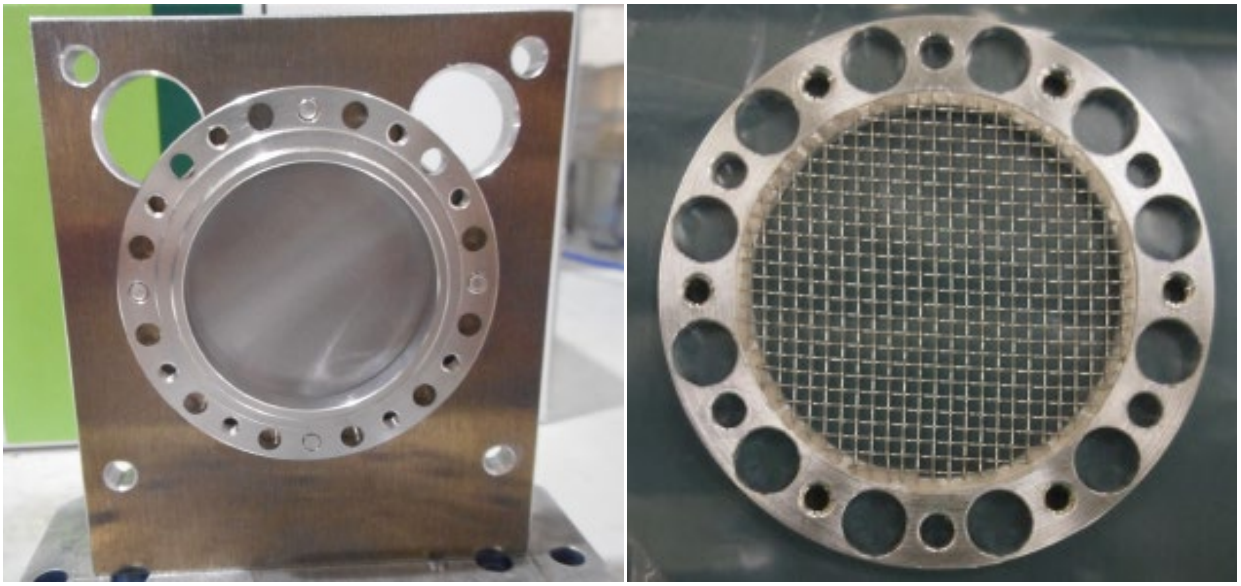

Figure 1 Picture of the Be window (CM placed on the holder) and the stainless mesh (FM attached to the flange). The inner diameter of both is about 29 mm [5].

Table 1 : Summary of GV Be window materials and dimensions.

Description	Material	Geometry	Thickness	Comments
Be window	Be	Thickness non-uniformity of ~10%.	~270 μm	
Stainless mesh	Stainless steel (SUS304)	1/20 inch pitch wire mesh	Wire thickness = 0.20 mm	Mesh opening width is 1.27 mm – 0.20 mm = 1.07 mm. Open fraction = 71%

2.2 Versions of the hardware components used for calibration

Be window: We fabricated three models for the Be window made from the same lot of Be. They are flight model (FM), FM spare, and calibration model (CM). We used FM for the measurement at KEK both for the energy and spatial dependence of its X-ray transmission. We used the CM for two additional transmission measurement at HiSOR and TMU for improving the modeling. The details of the additional measurements are given in [1].

Stainless steel mesh: The FM mesh was not available for the calibration test period, thus we utilize the mesh made for the engineering model (EM) Dewar of SXS. The design has been changed between SXS and Resolve, which is included in the modeling performed to create the CalDB curves.

2.3 Geometry changes from SXS

The geometry of the Resolve GV structures is shown in Figure 2 and Figure 3 [5],[6].

Two primary changes were made between Resolve and SXS [7]. The flange shape was changed beneath the Be window, so that the effective aperture is 29.0 mm for Resolve instead of 27.0 mm for SXS (Figure 2). The cross structure at the center was removed (Figure 3). These make the aperture shape simpler and decrease the systematic uncertainty on the x-ray transmission caused by these parts in the middle of the X-ray optical path.

Section 4.3 (Figure 16) provides a schematic showing the three-dimensional layout of gate valve components used to model the Resolve gate valve structure in the CalDB.

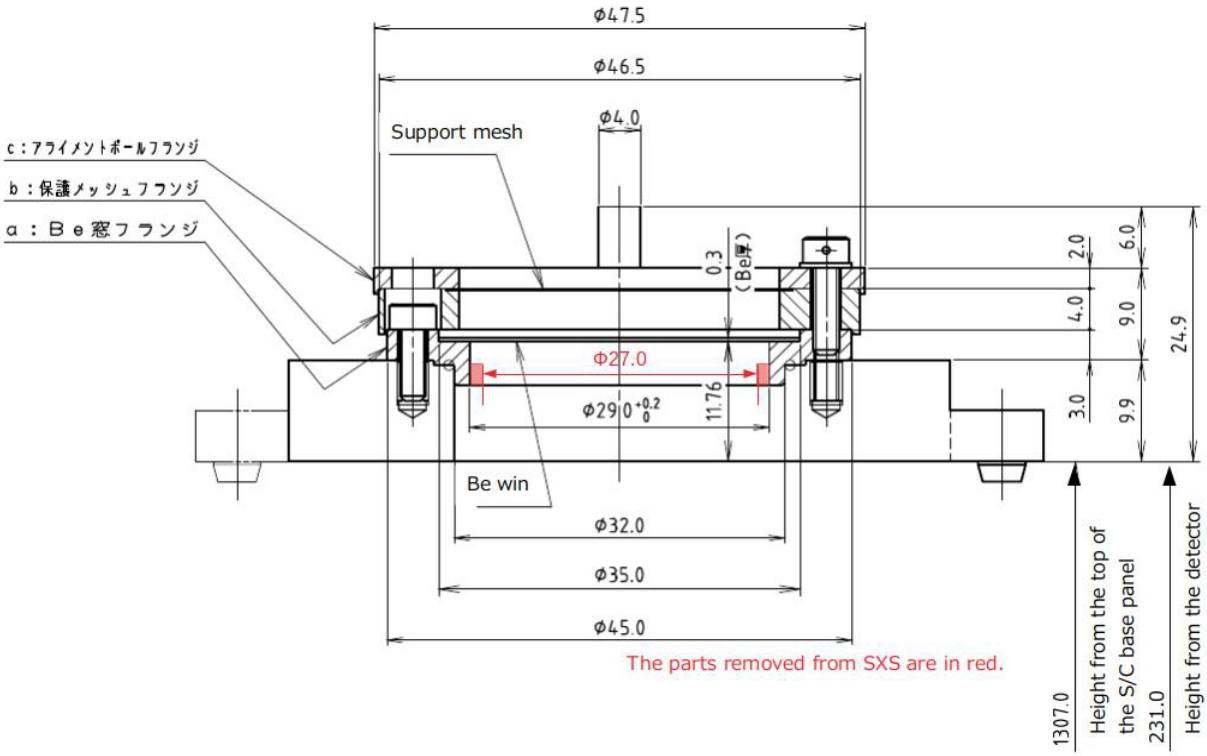

Figure 2 Drawing of the GV and its height from the spacecraft base panel [5] and the detector plane [6].

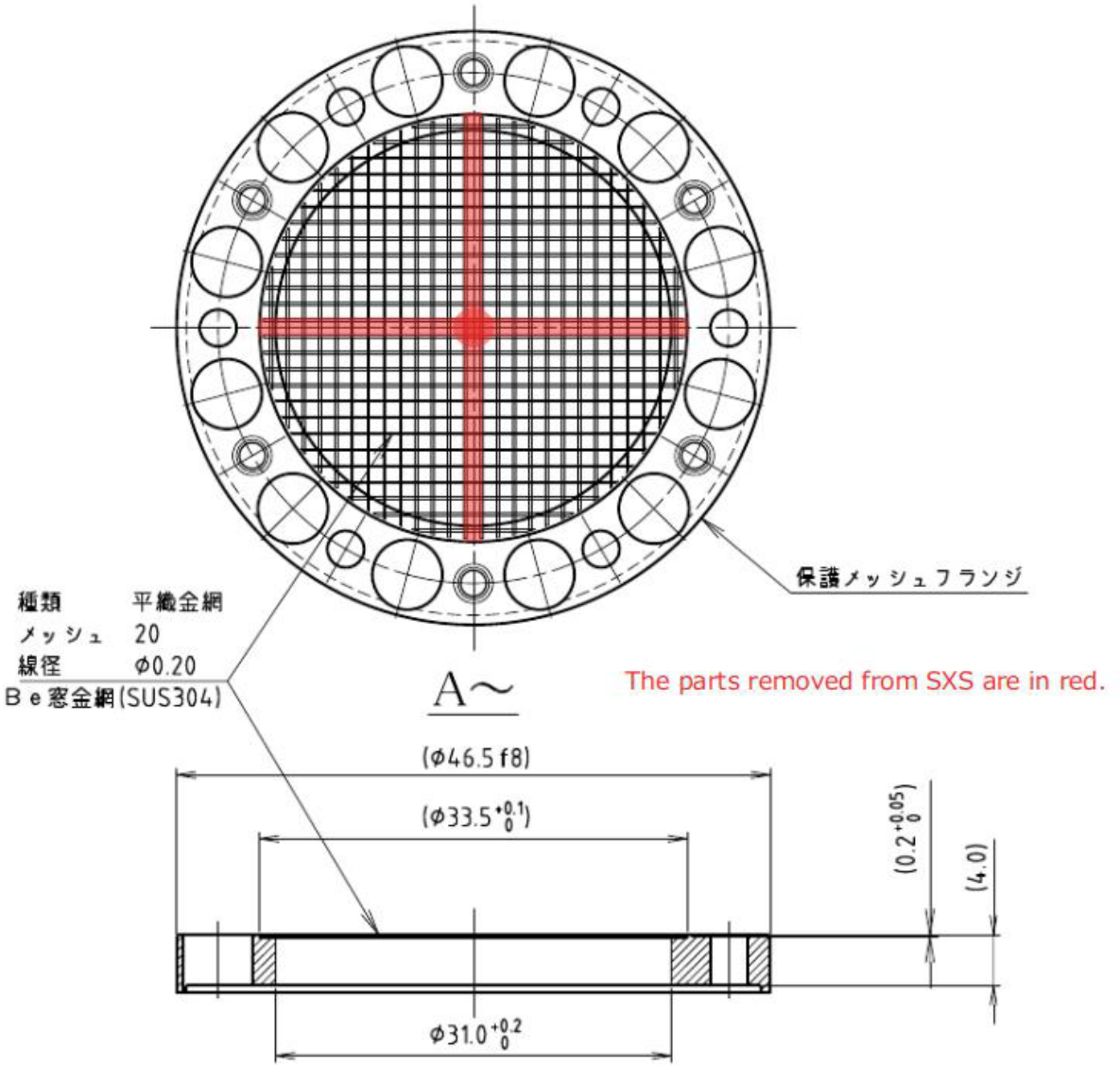

Figure 3 Drawing of the stainless mesh with the flange [5].

3 Ground calibration measurements and modeling

3.1 Energy dependence of the X-ray transmission of the Be window

3.1.1. SETUP AND RESULTS

X-ray transmission of the Be window was measured using the FM Be window at KEK Photon Factory (PF) from June 13 to 23, 2019. We used the beam lines BL7C and BL11B, where the operating energy ranges are 4.0-12.0 keV and 2.1-5.0 keV. The synchrotron X-rays are monochromatized using a Si (111) double crystal monochromator (DCM). We used a beam spot size of 1.0 mm x 1.0 mm to measure three positions on the Be window. They are at the center of the window and at two positions 6.5 mm off-center (top and bottom).

Figure 4 shows schematic drawings of the setup for measurements [2]. In the BL11B experiments, we attached our vacuum chamber to the beam line and installed the Be window and a photo diode inside to prevent absorption by the atmosphere as shown in Figure 5. The incident X-ray was measured using a Ti foil as a front detector provided by the facility. In the BL7C experiments, we measured incident X-rays and transmitted X-rays by two ion chambers filled with N_2 gas provided by the facility in front and back of the Be window placed in the air. We removed higher order X-rays with a focusing double mirror at the BL7C.

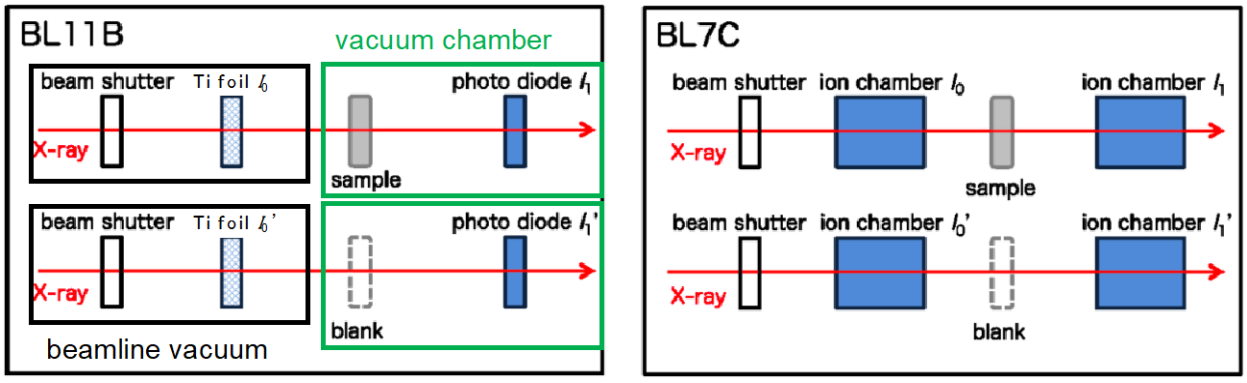

Figure 4 Schematic drawings of the setup for measurements at BL11B and BL7C [2].

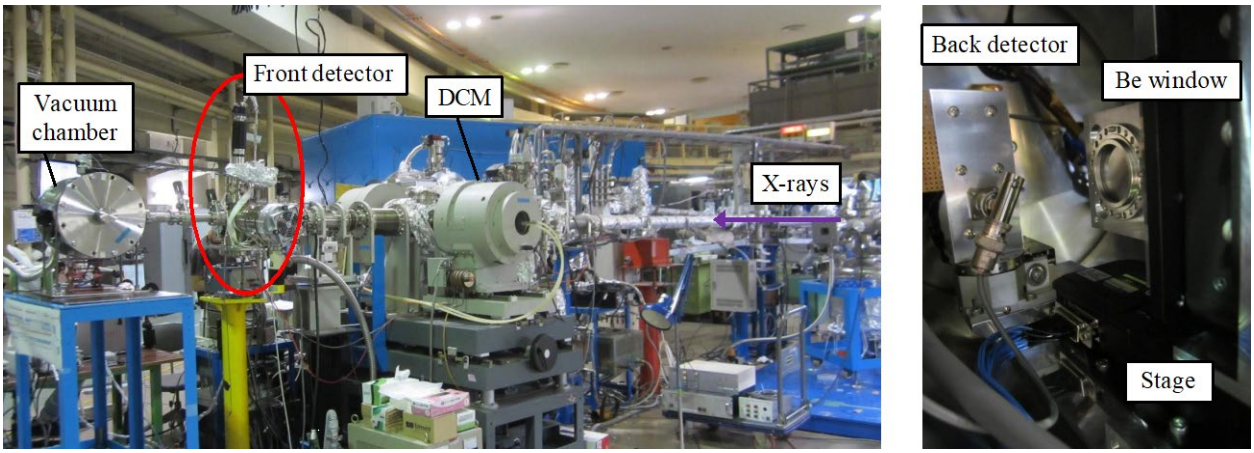

Figure 5 *left*: The photo of the BL11B. X-rays come from the other side to the vacuum chamber. *right*: The interior of the vacuum chamber. Be window and a photo diode as a back detector are installed.

In both experiments, we measured the intensity of the incident and transmitted X-rays with and without the Be window. Let's assume that $I_0(E)$ and $I_1(E)$ are the incident and transmitted X-ray intensities with the Be window, and $I'_0(E)$ and $I'_1(E)$ are those without the Be window at a given energy E. We derived the transmission by Equation 1. With this double normalization, we can correct for variation in the incident beam as well as the energy dependence caused by the measurement setup. We used a step size of 2 eV.

$$T(E) = \frac{I_1(E)/I_0(E)}{I'_1(E)/I'_0(E)} \quad (1)$$

The upper panels of Figure 6 show derived transmission curve of the top position of the Be window in 2.1-4.5 keV at BL11B (left) and in 4.0-12.0 keV at BL7C (right). The lower panels show the ratio to the model assuming photoelectric absorption by Be of a 250 μm thickness. Anomalous transmission increase seen below 2.5 keV at the lower panel is likely caused by the contamination of higher-order X-ray reflection at the DCM. Therefore, we ignore the transmission results below 2.5 keV for the following analysis.

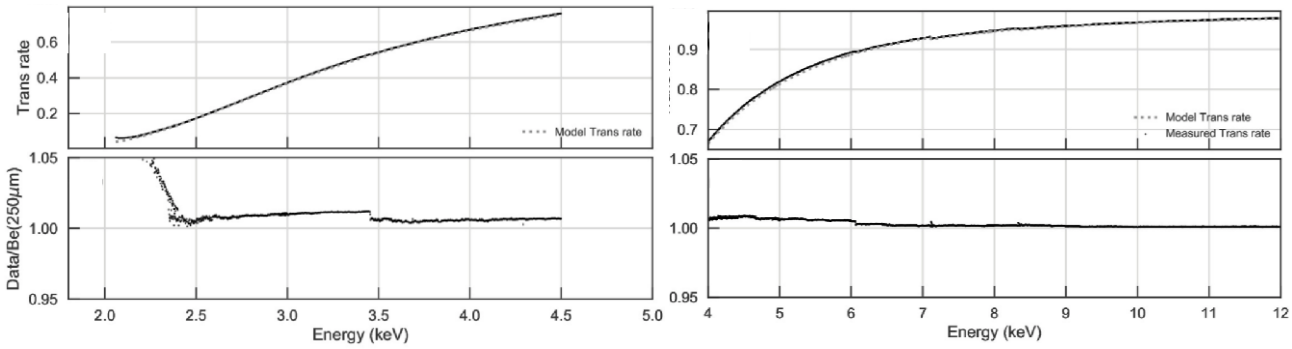

Figure 6 Upper: A model transmission curve assuming photoelectric absorption by Be of a 250 μm thickness and the transmission measured at the top position of the Be window obtained at BL11B (left) and BL7C (right).
Lower: The ratio of the measurement curve to the model curve.

3.1.2. MODELING

First, we investigated the contamination by minor elements. We identified some features in the lower panel of Figure 6 with photoelectric absorption edges by Fe-K, Ni-K, Cr-K, Mn-K and Cu-K. We derived their aereal densities by local fitting and summarize the result in Table 2. These features were also identified in the SXS Be window.

Table 2 Best-fit parameters of minor elements based on the transmission measurements of the FM window.

Minor Element	Edge Energy [eV]	Fitting Energy Range [eV]	Best-fit areal [a] density σ_{minor} [μg/cm^2]	Reference areal [b] density σ_{minor} [μg/cm^2]
Cr	5989	5500 - 6050	0.8 ± 0.1	1
Mn	6539	6510 - 6900	< 0.2	1
Fe	7112	7000 - 7500	11.4 ± 0.2	9
Ni	8333	8200 - 8450	7.7 ± 0.2	5
Cu	8979	8800 - 9180	0.7 ± 0.1	1

[a] The uncertainties are at the 1σ confidence level.
[b] The values are derived from the fraction of materials measurements by Materion Corp.

We also detected other edge-like features at 3460 eV, 6057 eV, etc. They are physically interpreted by the Bragg diffraction by the Be window [2], [3], [13]. Here, the Be window is a poly-crystal, in which a part of the material satisfies the Bragg condition at any given energy. An ideal case is called the powder diffraction and the diffracted X-rays form a ring called the Debye-Scherrer ring. Hereafter, we call these edge-like features as Bragg Diffraction Features (BDFs).

When the incident X-ray energy satisfies the Bragg condition (Equation 2) for the lattice spacing d_{hkl} of the Miller index (hkl), X-rays are scattered into a Debye-Scherrer ring. The ring disappears when the incident energy becomes lower than $E_{hkl}(\theta = \pi/2)$, as the scattered angle cannot exceed $2\theta = 180°$. This causes a discontinuity in the measured transmission curve at $E_{hkl}(\theta = \pi/2)$ of all Miller indices except for those with systematic absence.

$$E_{hkl}(\theta) = \frac{hc}{2d_{hkl}\sin\theta} \tag{2}$$

We took the following approach in modeling the BDFs. We used the thickness of the photoelectric absorption, coherent scattering, and incoherent scattering as phenomenological fitting parameters. The mass attenuation coefficients for the three interactions was fixed to the values by the NIST database. This approach was motivated by the fact that the scattering cross section effectively changes in lattice from the values in atoms in dynamical diffraction theories [10]. Considering the underlying physics [1], [11], we changed the coherent scattering thickness in a step-wise manner at all BDFs. In between two BDFs, we assumed that the thickness
is proportional to the inverse square of the incident energy (Figure 11). This is derived from the discussion [12] on the cross section of the power diffraction as

$$\frac{d\sigma}{d\Omega} = N_c\left(\frac{d_\tau^3}{v_0}\right)M_\tau|F(\tau)|^2\frac{\tan\theta}{2\pi}\delta(\gamma), \tag{3}$$

in which N_c is the number of unit cells in the powder crystal, v_0 is the volume of a unit cell, τ is the reciprocal vector corresponding to a Miller index, $F(\tau)$ and M_τ are respectively the structure factor and the reflection multiplexity factor for the reflection τ , d_τ is the lattice spacing. The Bragg condition is met as $hc/E = 2d_\tau\sin\theta$. The angle $\gamma = 2\theta$ and $d\Omega = 2\pi\sin\gamma d\gamma$. The Equation 3 is derived for the constant-wave case, but it applies to the constant-energy case as well as wavelength-dispersive case with variable conversions. The scattered photon counts per second integrated over the entire solid angle (or entire energy range through the Bragg condition) is then given by

$$P_\tau(E) = \int dE'\frac{d\sigma}{d\Omega}\frac{d\Omega}{dE'}\Phi(E') = N_c\left(\frac{d_\tau}{v_0}\right)M_\tau|F(\tau)|^2\Phi(E)\frac{h^2c^2}{4E^2} \tag{4}$$

in which $\Phi(E')$ is the incident photon counts per second per unit area per energy bin. From these, $P_\tau(E)/\Phi(E) \propto E^{-2}$, which translates to the thickness dependence on E when the scattering depth is optically thin. The thickness was left constant at energies above ~9 keV, in which numerous BDFs exist. This is different from the SXS GV modeling, in which the BDFs were only fitted locally [2]. Our model consists of the following components:

- Photoelectric absorption and incoherent scattering by the bulk Be to account for the overall shape of the transmission curve.
- Photoelectric absorption by minor elements (Ni, Fe, Cu, Mn, Cr) to account for the absorption edges.
- Coherent scattering by Be with a step-wise changes in thickness to account for the BDFs.

The total transmission is given by

$$T_{\mathrm{Be}}(E) = T_{\mathrm{Be,photo+inc}}(E) * T_{\mathrm{minor,photo}}(E) * T_{\mathrm{BDF}}(E), \quad (5)$$

where $T_{\mathrm{Be,photo+inc}}(E)$ is the transmission due to the photoelectric absorption and incoherent scattering by the bulk Be expressed as:

$$T_{\mathrm{Be,photo+inc}}(E) = \exp(-t_{\mathrm{Be,photo+inc}} * \rho_{\mathrm{Be}} * (\mu_{\mathrm{Be,photo}}(E) + \mu_{\mathrm{Be,inc}}(E))). \quad (6)$$

Here, $t_{\mathrm{Be,photo+inc}}$ is the thickness of the bulk Be common to the photoelectric absorption and the incoherent scattering, ρ_{Be} is the Be density, and $\mu_{\mathrm{Be,photo}}(E)$ and $\mu_{\mathrm{Be,inc}}(E)$ are, respectively, the mass absorption coefficient of photoelectric absorption and incoherent scattering as a function of incident X-ray energy E obtained by NIST database. $T_{\mathrm{minor,photo}}(E)$ is the transmission due to the photoelectric absorption by the minor elements, which is calculated by

$$T_{\mathrm{minor,photo}}(E) = \prod_{\mathrm{minor}} \exp(-\sigma_{\mathrm{minor}} * \mu_{\mathrm{minor,photo}}(E)). \quad (7)$$

where σ_{minor} is the areal density of the minor elements. We modeled the transmission of the BDFs by

$$T_{\mathrm{BDF}}(E) = \exp(-t_{\mathrm{Be,coh}}(E) * \rho_{\mathrm{Be}} * \mu_{\mathrm{Be,coh}}(E)). \quad (8)$$

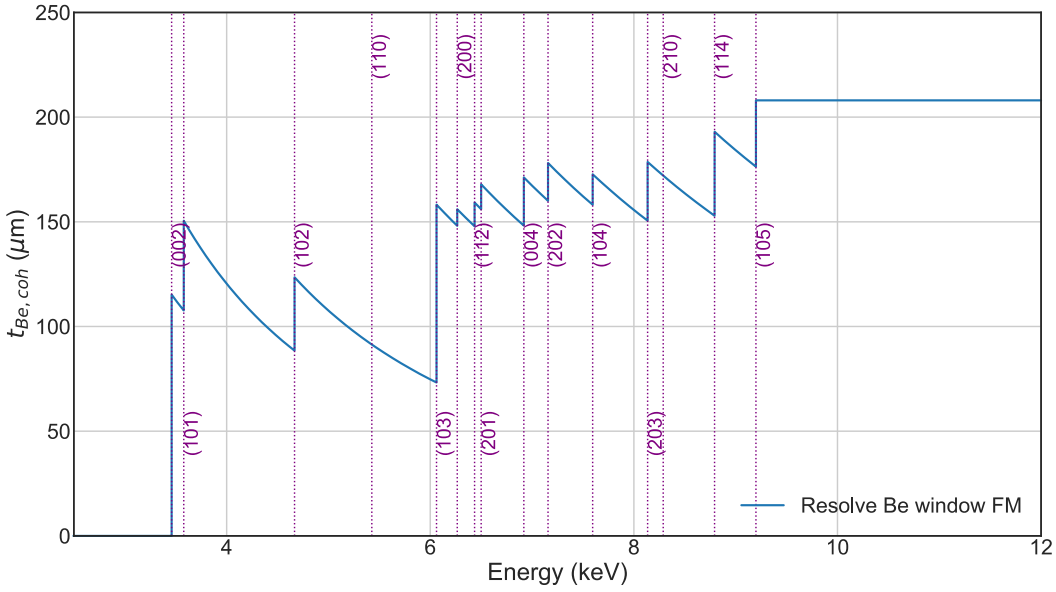

Figure 7 The best-fit coherent scattering thickness by Be. Purple lines represent the energies at which the BDFs appear, and the numbers in parentheses represent the crystal surfaces (*hkl*) that cause the BDF.

Figure 8 shows the best transmission model for the Resolve FM Be window. We achieved less than 0.2% discrepancy between the measurement and the model over a wide range of energy, which is much smaller than the calibration requirements.

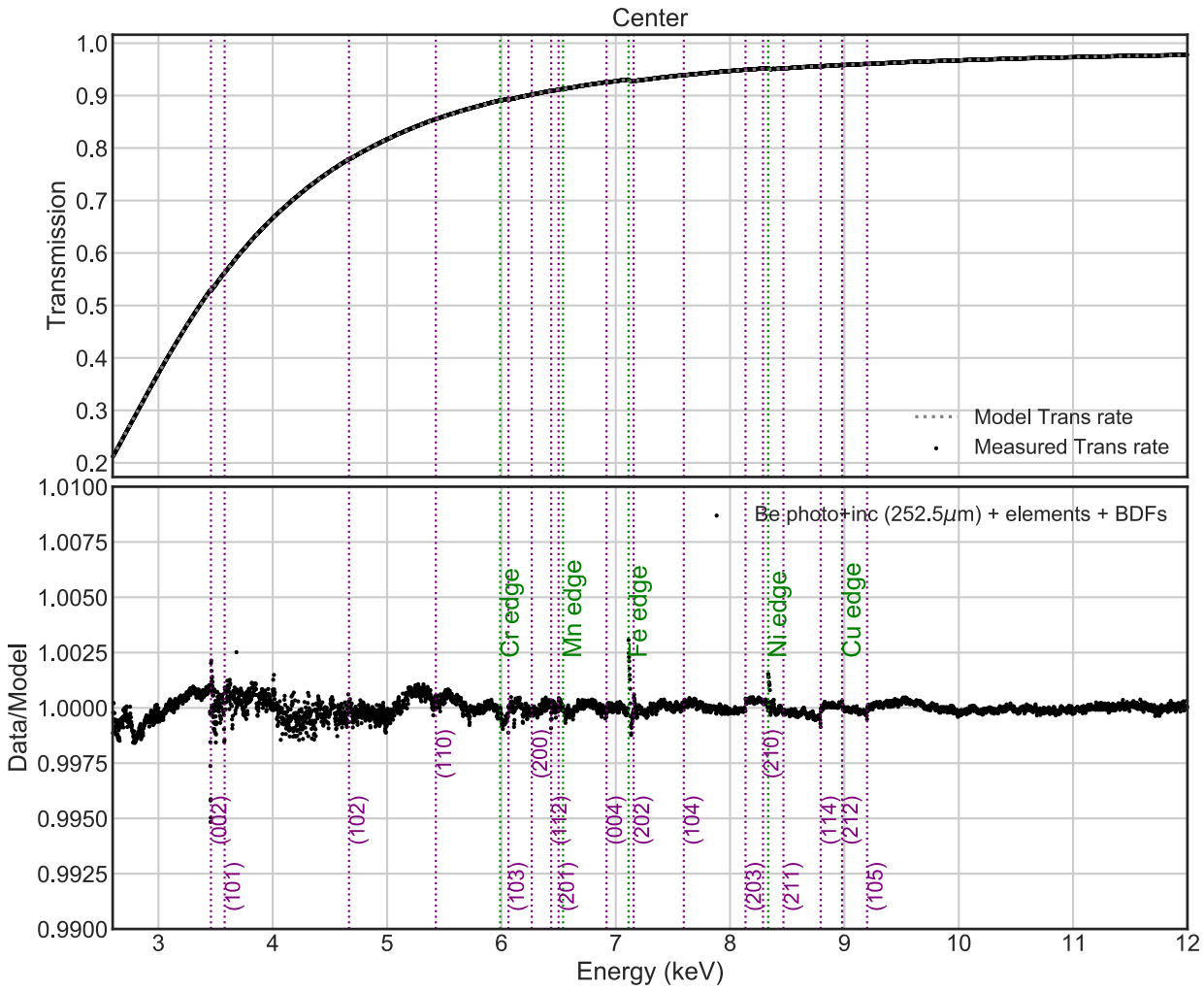

Figure 8 Best-fit transmission model of the FM Be window in 2.6-12.0 keV. The edges by the contaminants are shown in green, while the BDFs of the labeled Miller index is in purple.

3.2 Energy dependence of the X-ray transmission of the stainless mesh

3.2.1. SETUP AND RESULTS

X-ray transmission measurements of the stainless mesh were performed using the 30 m X-ray beam line at JAXA ISAS [9] from February 4 to 19, 2019. At the time, the Resolve FM stainless steel mesh had not yet been manufactured, thus we used the SXS EM mesh. The SXS mesh has the same design as Resolve's. Figure 9 shows the schematic of the beamline. X-rays from an X-ray generator illuminated one of five metal targets, Ti, Cu, Pt, Mo or Ag. The fluorescent and scattered X-rays were further monochromatized using a Ge (220) double crystal monochromator (DCM). With a slit the beam size was adjusted to be 2.0 mm x 2.0 mm, which is comparable in size with the mesh spacing (Table 1).

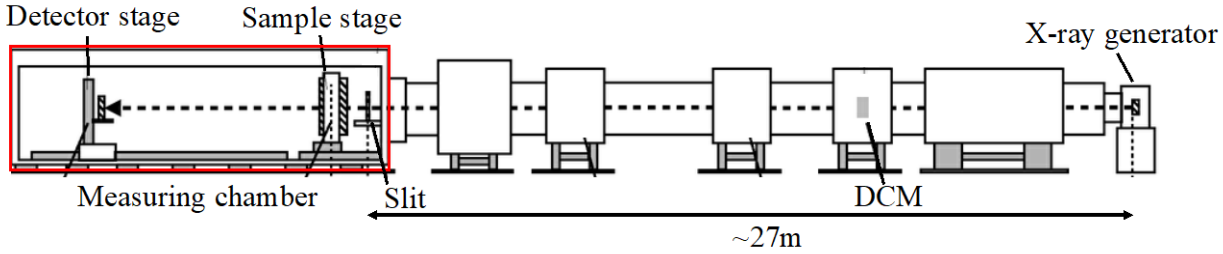

Figure 9 Schematic of the ISAS beam line. The distance between X-ray generator and slit is approximately 27 m. The slit, sample stage and detector stage are installed in the measurement chamber.

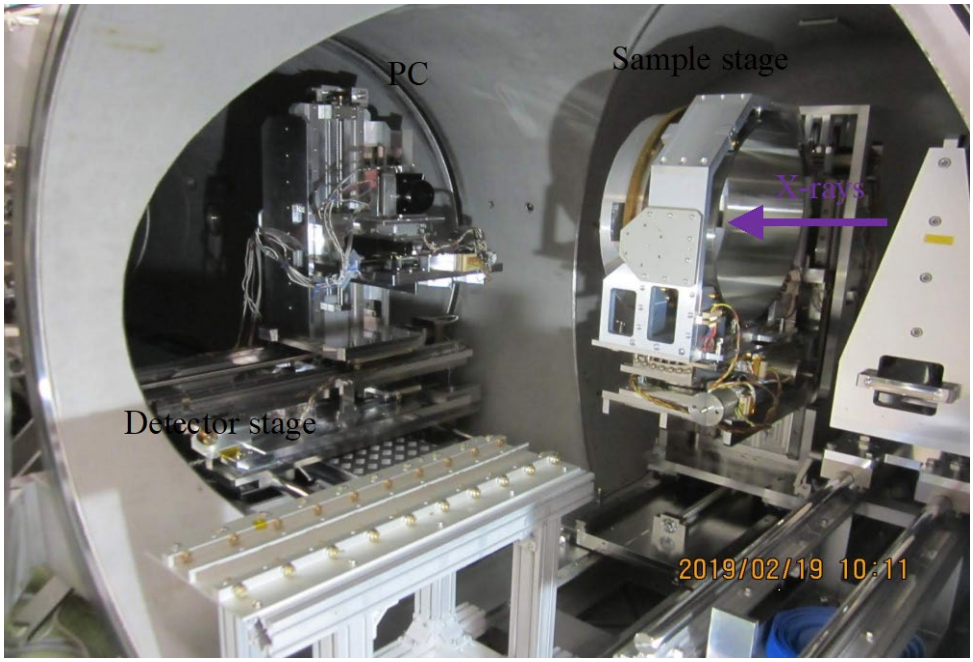

Figure 10 The interior of the measurement chamber.

We performed a raster scan to average the transmission over the entire mesh. The raster pattern is a zig-zag composed of several lines in each quadrant. Because the Resolve measurements were made on the SXS mesh in an assembly that contained a cross structure (see Figure 3), both the cross and the rim were avoided in the raster scan. The raster was repeated several times to accumulate sufficient statistics. For each scan of a line, we obtained an integrated X-ray spectrum with a proportional counter (PC) on a detector stage of the measurement chamber (Figure 10). The detector stage and the sample (mesh) was moved synchronously, so that the parallel X-rays illuminate the same spot of the detector.

X-ray spectrum with and without the mesh was measured, which we call the transmitted and direct X-rays. We calculated the transmission of the mesh by taking the ratio between the transmitted and direct photons (Table 3).

Table 3 Scan number, total exposure time and total detected photons of transmitted (sample ON) and direct (sample OFF) X-rays, and calculated transmission and measurement error considering systematics and statistics.

Line	Energy [keV]	Sample	Scan Number[a]	Total Exposure [sec]	Total Photons [counts]	Transmission [%]	Error [%]
Ti Kα	4.51	ON	8	1866.3	2562596	72.71	±0.62
		OFF	10	3627.8	6850815		
Cu Kα	8.05	ON	8	1856.7	200030	71.74	±0.90
		OFF	10	3601.7	540877		
Pt Lβ	11.07	ON	8	1858.0	422722	71.52	±1.46
		OFF	10	3605.6	1149485		
Mo Kα	17.48	ON	16	3712.8	211733	72.32	±2.28
		OFF	10	3601.6	285442		
Mo Kβ	19.61	ON	48	11136.2	122811	73.58	±2.80
		OFF	20	7200.1	109824		
Ag Kα	22.17	ON	8	1861.2	270694	76.38	±1.31
		OFF	10	3613.6	686769		

[a] A measurement of transmitted X-rays over one quadrant is considered one scan. We need four scans to measure transmitted X-ray photons on the whole mesh. One measurement of the direct X-rays takes about 60 seconds. We call six measurements for about 360 seconds as one scan to reduce fluctuations of incident X-rays and gain in the PC.

3.2.2. MODELING

In Figure 11, the measured transmission curve is shown with the red points, whereas the model curve adopted in the SXS CalDB [13] are with the blue curve. The mesh is made of SUS304, which is modeled as 70% Fe, 20% Cr, and 10% Ni. The transmission is modeled by a product of the photoelectric and scattering attenuation of these materials.

The model curve of the SXS CalDB found to be inconsistent with the measurements, in particular, for the low energy side end as Ti Kα (4.51 keV) and the high energy side end as Ag Kα (22.17 keV). One reason is that the cross section of the mesh wire was assumed a square with 0.2 mm x 0.2 mm. The average depth is 0.2 mm at any point of the wire. However, in fact, the cross section is round, hence the average depth is smaller by π /4. The transmission is non-linear to the depth, so we did numerical integration assuming that the wire depth is $2\sqrt{t^2/4 - x^2}$ at x ($< t/2$) away from the center of the wire with a size of t. From the total mass attenuation coefficient of a constituent metal $\mu_{\mathrm{tot,metal}}(E)$, we derived the attenuation coefficient $\alpha(E)$ as

$$\alpha(E) = \sum_{\mathrm{metal}} A_{\mathrm{metal}} * \rho_{\mathrm{metal}} * \mu_{\mathrm{tot,metal}}(E) \quad (9)$$

where A_{metal} is the abundance ratio and ρ_{metal} is the mass density of metal elements (Fe, Cr, Ni). The transmission of the stainless mesh $T_{\mathrm{mesh}}(E)$ was then calculated as:

$$T_{\mathrm{mesh}}(E) = f + (1-f) * \int_0^{\frac{t}{2}} \exp\left(-2\sqrt{t^2/4 - x^2} * \alpha(E)\right) dx \quad (10)$$

where f is the fraction of the open area of the mesh.
First, we fixed f to 0.71 based on the drawing (Figure 3), which is shown with the orange curve in Figure 11. This is still inconsistent with the measurement. We recognize some uncertainty in the estimate of f, which was treated as a free parameter. The best-fit value was 0.723±0.003. The resultant model is shown with the green curve in Figure 11, which is consistent with the measurement. We adopt this improved model for the Resolve CalDB.

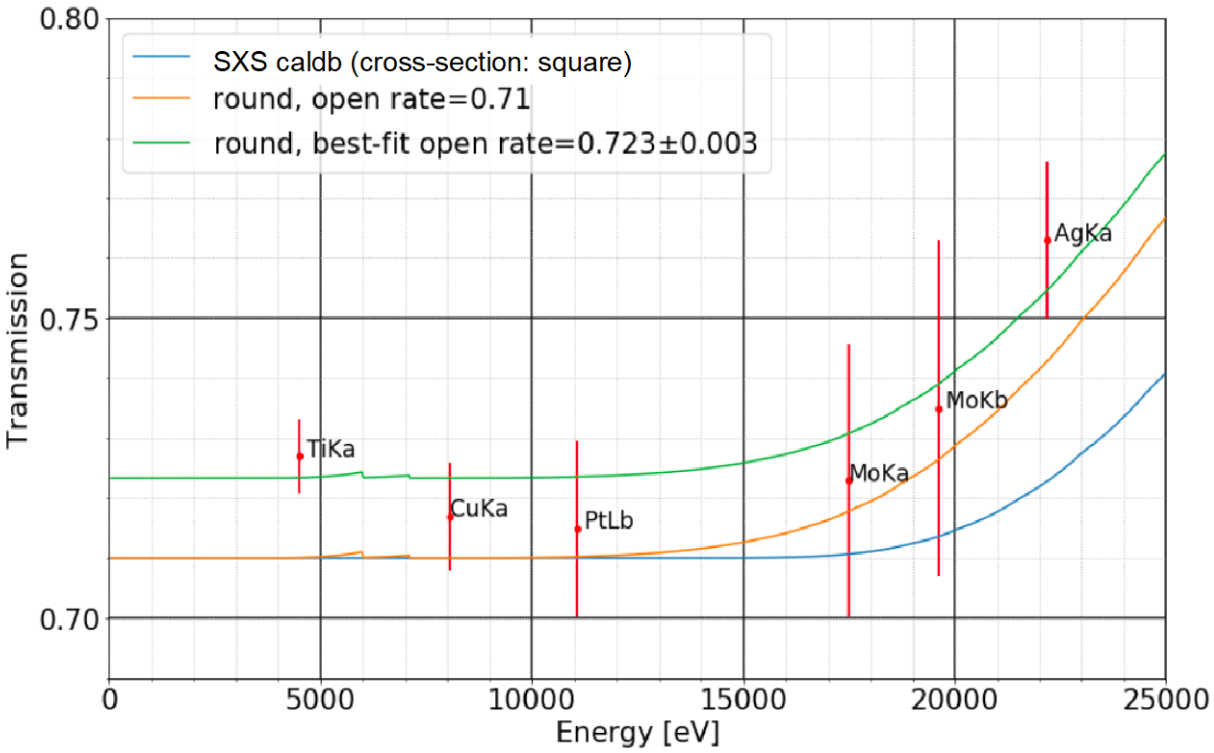

Figure 11 Comparison of three transmission models for the stainless mesh. Red points describe the measurement results with error. Blue, orange, green line shows SXS CalDB, round cross-section model which has 71% open area and *Resolve* CalDB model with 72.3% open area. ("Open rate" used in the legend is equivalent to open fraction.)

3.3 Spatial dependence of the X-ray transmission of the Be window

3.3.1. SETUP AND RESULTS

It is known from the Astro-E2 XRS program that the thickness of the Be window has some non-uniformity–based on measurements at Mo-L, Ti-K, and Cu-L energies, the Astro-E2 Be window showed a thickness gradient of 5%. This led us to evaluate the spatial non-uniformity of the Resolve FM Be window using the KEK photon factory BL-11B. The setup is the same as in Section 3.1.

We measured the X-ray transmission at a set of fixed energies over the entire Be window. We chose four energies: 2700, 3000, 3456, and 4000 eV. The scan was continuous in the horizontal direction with a speed of 500 μm/s and stepwise in the vertical direction with a step size of 1mm. For each horizontal scan, we obtained reference transmission without the Be window for 10 s. The transmission at each time was derived using the Equation 1, which is converted to a map by matching the time with the position.

shows the two-dimensional maps of the transmission of the FM Be window. The figures are aligned to the DWR coordinate: i.e, +X, +Y directions in the figure are aligned to DWR+X, DWR+Y and to SAT+X and SAT+Y. These maps were faced in the direction viewed from the incident X-rays both in the experiment and also to the in-orbit setup. For all energies, transmission at the lower left of the Be window is higher than that at other parts. It is conceivable that the lower left part became thinner during rolling process of the Be.

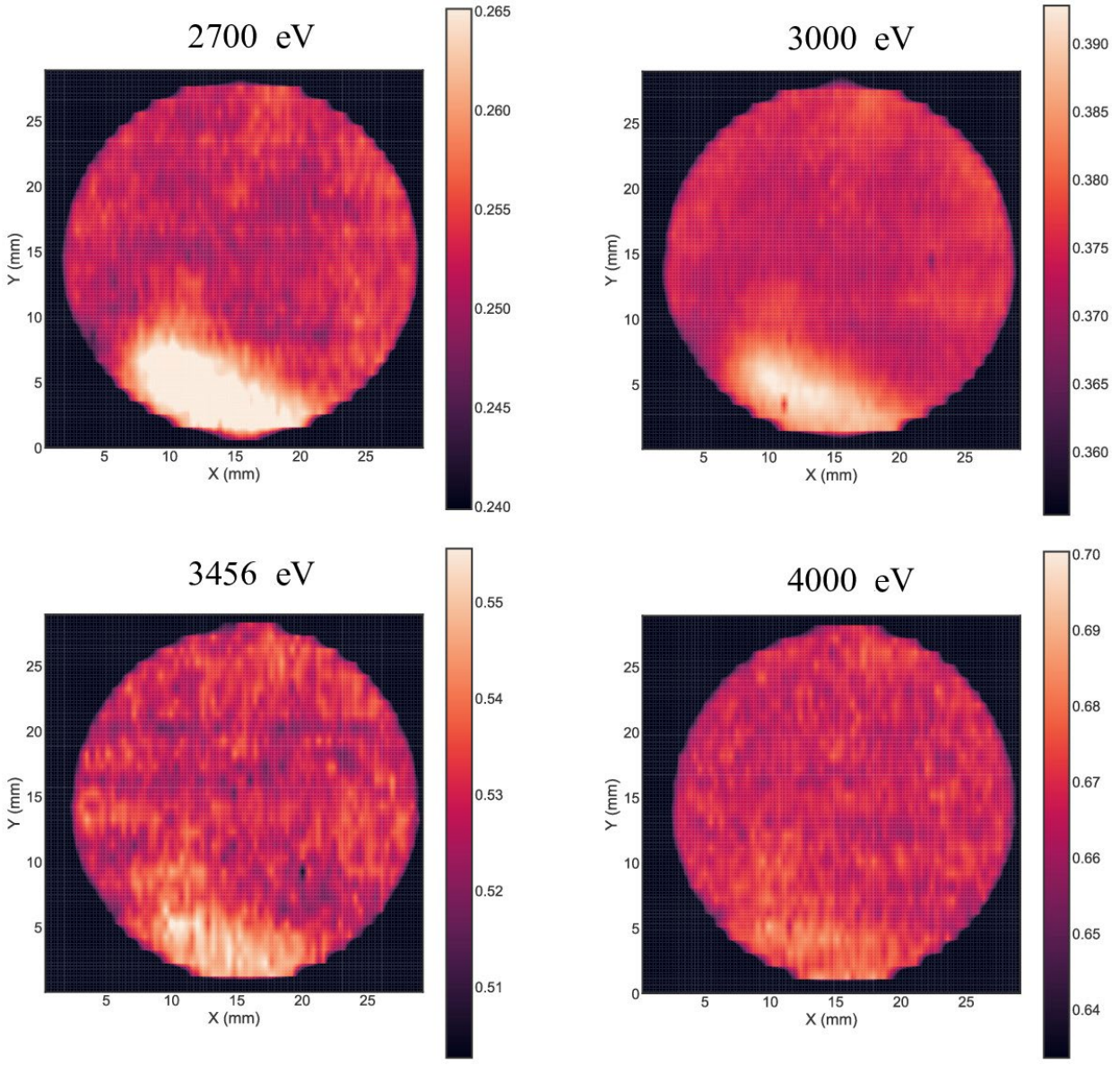

Figure 12 Transmission of the FM Be window at four selected energies, highlighting the spatial non-uniformity.

3.3.2. MODELING

In order to perform raytracing simulations at arbitrary energies to assess the effects of spatial non-uniformity, it is necessary to convert the transmission images into thickness maps. However, the perimeters of all the images had significant artifacts that would have adverse and unphysical effects on raytracing results. The 3 keV image appeared to be the least affected in this respect, so we adopted that image for repairing and generating a thickness map. The bulk of the pixels in the

image have a transmission higher than 0.37, and pixels with a lower transmission are associated with the anomalous edge effects. We repaired the image by replacing pixels with transmission values less than 0.37 by the mean transmission of pixels inside a circle with a radius of 12.5 mm, centered on the center of the Be filter.

Using Henke data (Ref 16), and a Be density of 1.8 g cm^{-3}, we generated a thickness map from the repaired image. Figure 12 shows a histogram of the thickness distribution of pixels in the map generated from the repaired image (black), and it is directly compared with the corresponding histogram from the unrepaired image (red).

A raytracing study in the 0.1-30 keV energy range, performed using the thickness map based on the repaired image, showed that above ~2 keV the effects of spatial non-uniformity in the Be filter thickness are negligible, and below ~1 keV, the absolute transmission probability of the Be filter is negligible (<10^-8), regardless of the thickness variations. For an on-axis point source, between 1 to 2 keV, the effect of the spatial non-uniformity is <2.5%. However, we examined the effect of the spatial non-uniformity on the PSF, and found that it is larger than the effect on the transmission, but <10% within 0.5' of the PSF core, below 2 keV. A related effect, the Resolve pixel-to-pixel relative counts, can be affected by as much as 8% below 2 keV. As with the transmission probability, above 2 keV, the effects of spatial non-uniformity on the PSF are negligible. However, the effects of spatial non-uniformity are larger for off-axis sources compared to an on-axis point source.

Nevertheless, it was decided that for the pre-launch CalDB file, the single transmission curve for the Be filter (including the mesh) will be employed (see Section 4.3), and the spatial non-uniformity capability of the CalDB file structure will be deployed later if necessary.

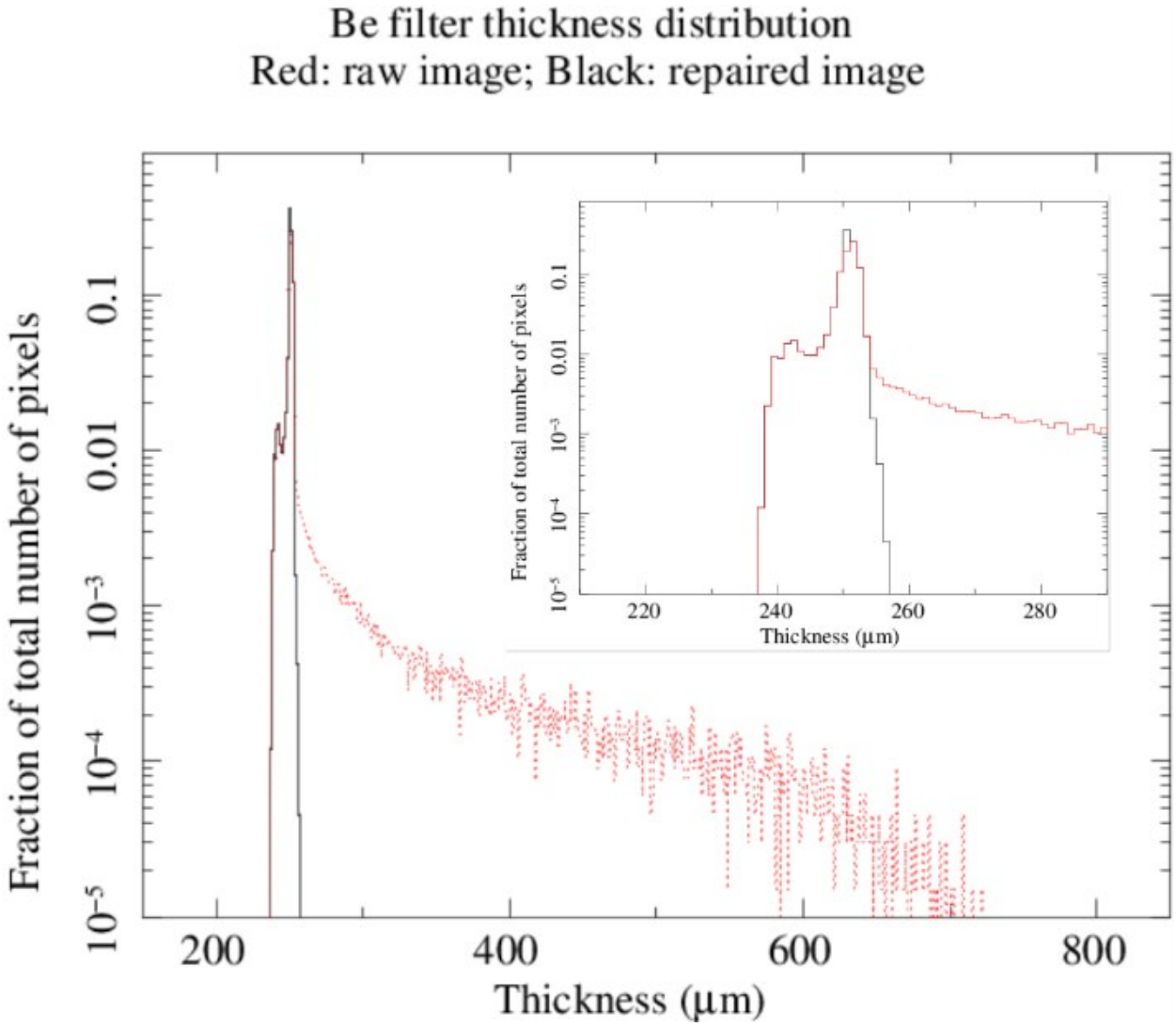

Figure 13 Histogram of the thickness at each spatial position of the measured data (red) and the part used for smooth modeling (black). The histograms were calculated using the 3 keV transmission maps (uncleaned and cleaned) and converting to thickness using literature mass-absorption data and a Be density of 1.85 g cm^{-3}.

4 CalDB Release 20210927

CalDB Filename	Validity date	File(s) as delivered	Delivery date	Comment
xa_rsl_gatevalv_20190101v002.fits	1/1/2019	Be_10-40000_0p25_Be253p5_coh_E1prop.dat Mesh_0723_10-40000_0p25.dat	3/30/2020	This CalDB file has remained the same through the pre-launch and Build 7 CalDB releases.

4.1 Data Description

The CalDB file has five extensions.

Extension 0 has a thickness map of the Be window that can be used to account for spatial non-uniformity, if needed. A Boolean keyword (FLMUNIF) in the header of the CalDB file indicates whether the map is to be used. FLMUNIFM=True indicates a spatially uniform Be window and FLMUNIFM=false indicates that a non-uniform image is supplied and should be used by the software. This version of the file has FLMUNIFM=True, and a dummy, uniform image that is for reference only, and not used.

Extension 1 provides the support structure transmission as a function of energy. For Resolve the support structure transmission is set to T(E) = 1.0 for all energies. (For SXS this was non-unity due to the cross structure.)

Extension 2 provides the gate valve window transmission, including the effects of the Be and the protective mesh. In the future, if there is a need to model a Be filter with spatial non-uniformity, separate transmission functions for the Be and mesh components are required. In that case, the Be transmission would be supplied for a Be reference thickness value (in mm), specified by keyword REFTHICK, so that it can be used in conjunction with extension 0, and the mesh transmission would be placed in extension 1. The transmission extensions have two columns: X-ray energy and transmission. The energy range is 10 to 40000 eV with a step size of 0.25 eV. The model is described in Section 4.2.1 and Ref. 11.

Extension 3 includes a pixel ratio map. Similar to extension 1, this is set to 1.0 for all pixels on Resolve, consistent with the three-hole model. For SXS this was not unity due to the effects of the support cross.

Extension 4 has the geometric data for the gate valve frame structure. The specifications of the three-hole gate valve model are contained in this extension.

Note: If spatial non-uniformity is required in the future, the image and keyword modifications above are sufficient for xmasim and the ARF generator when used in direct raytracing mode. However, if the spatial non-uniformity is required and the ARF generator is used in the (more common) indirect mode, the data in extensions 1 and 3 will have to be replaced with pre-calculated raytracing results, obtained with the non-uniform Be filter.

4.2 Energy dependence of gate valve window – Be and mesh (Extension 2)

4.2.1. MODEL

We used the best-fit model parameters for the Be window (Section 3.1) and the stainless mesh (Section 3.2) and multiplied them to derive the total transmission of the GV. Assuming that the Be window has a transmission of $T_{\mathrm{Be}}(E)$ and the stainless mesh has $T_{\mathrm{mesh}}(E)$, the combined transmission of the entire GV $T(E)$ is given by

$$T(E) = T_{\mathrm{Be}}(E)\{f + (1-f)T_{\mathrm{mesh}}(E)\}, \quad (11)$$

where f is fixed to the best-fit value 0.723. The models were extrapolated to cover the full range from 10 to 40000 eV and interpolated to fill in the 0.25 eV pitch (the original measurement pitch was 2 eV). The extrapolation and interpolation used the transmission model defined in Equation 11 and related equations in Ref [11]. Figure 14 shows the results.

Figure 15 shows comparison between the best-fit transmission model of the GV for Resolve (red) and SXS (blue). The lower panel shows the ratio of the two models. Below 4 keV, the ratio is larger than in other parts of the waveband likely due to the modeling of BDF. We can confirm some difference of the two models above 20 keV due to the change of the shape of the wire cross-section used to model the transmission of the stainless steel mesh.

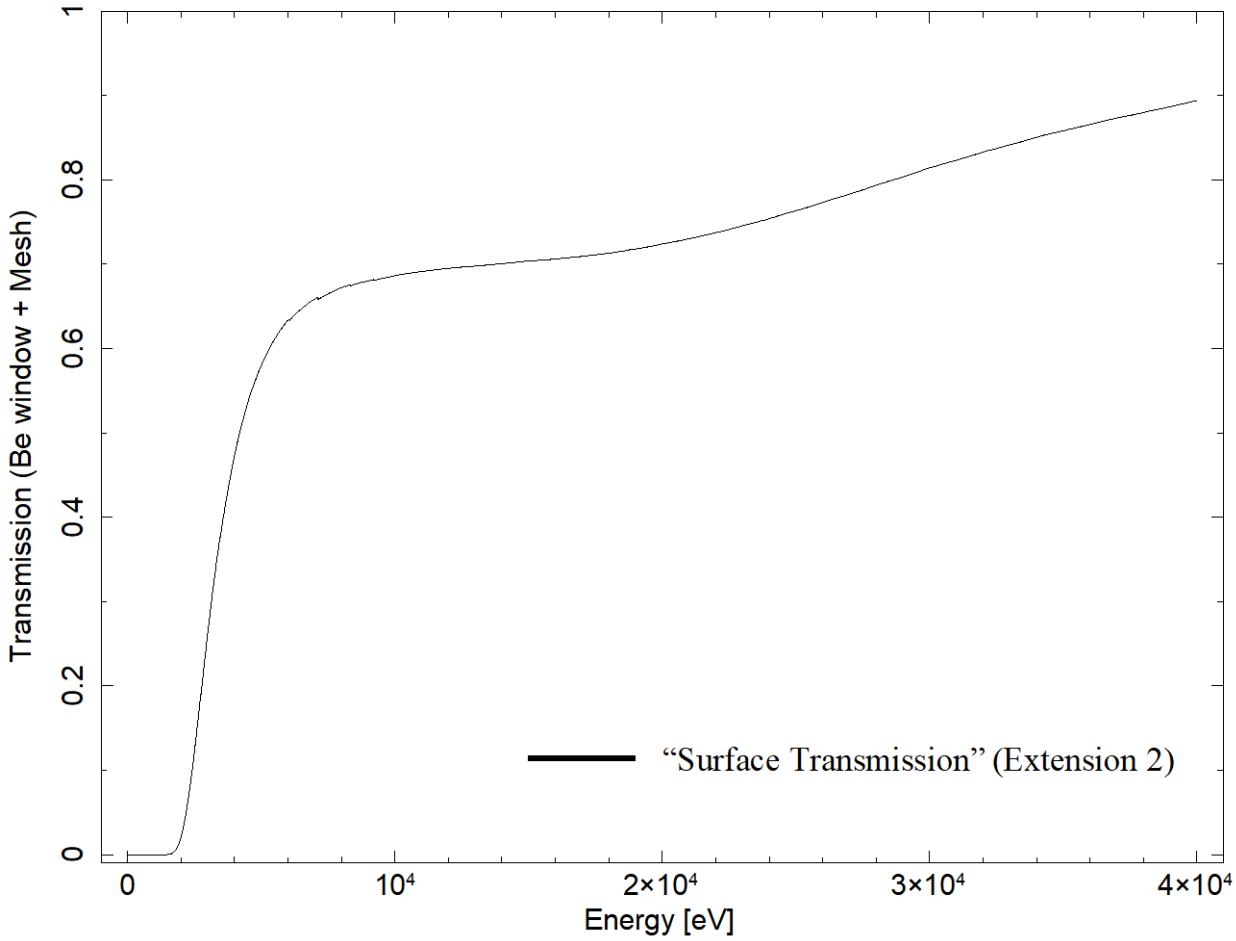

Figure 14 Transmission model of the GV.

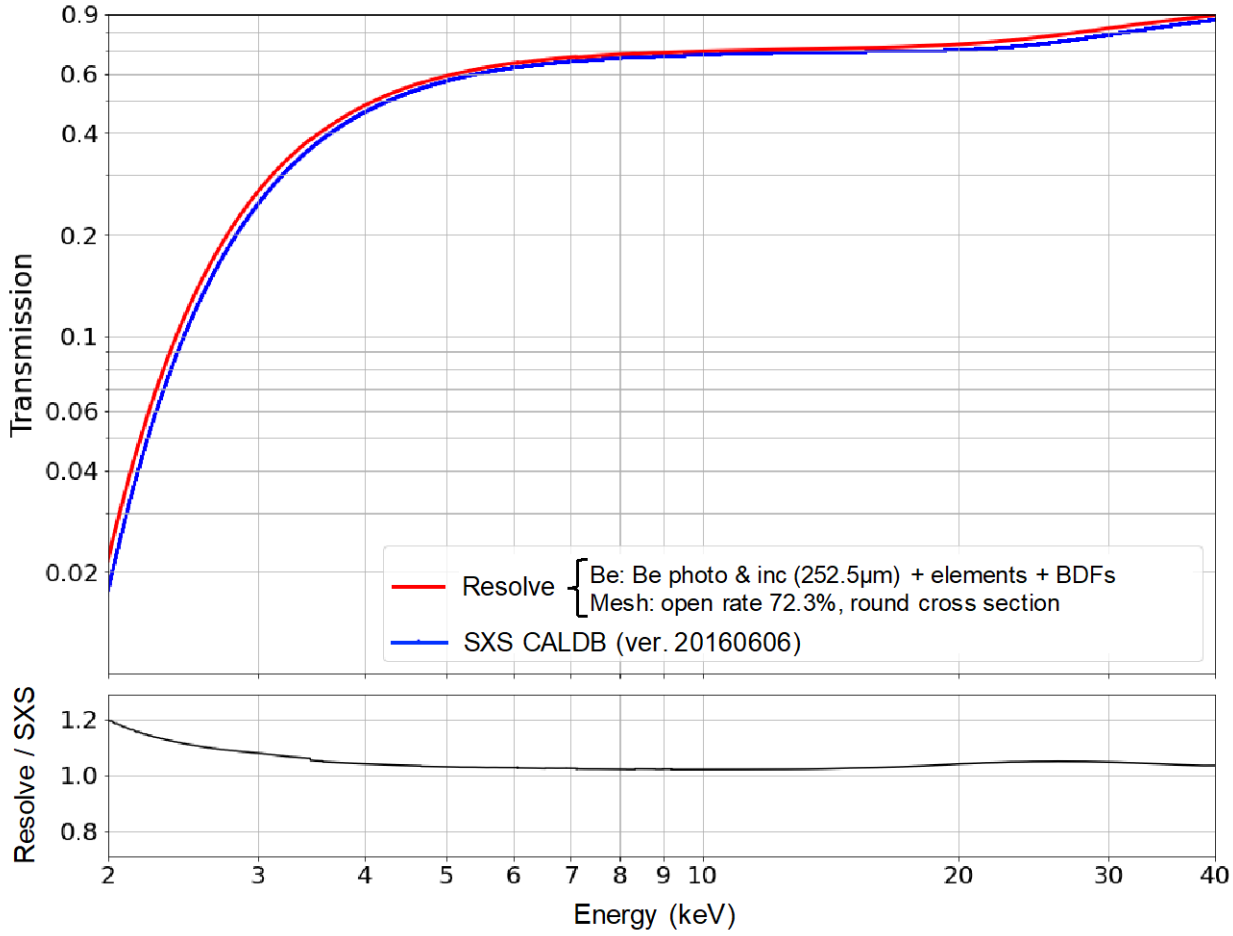

Figure 15 Comparison between the transmission model of the GV for Resolve (red) and SXS (blue, CalDB ver. 20160606) [13][14].

4.3 Spatial dependence and raytracing results (Extensions 1, 3, and 4)

The XRISM gate valve has a larger aperture than the Hitomi gate valve, and it also has no support structure blocking the beam (i.e., no "cross"), and this results in an on-axis effective area ratio with and without the gate valve support structure of unity at all energies between ~0.2 and 30 keV (established from raytracing with a point source). The same is true from raytracing results 5' off-axis for a point source. See Figures 16 and 17. This means that the function in extension 1 of the gate valve CalDB file can be unity at all energies.

Both the on-axis and off-axis results show that the pixel ratios (averaged over all energies between 0.2 and 30 keV) that are stored in extension 3 of the gate valve CalDB file can be unity for all pixels.

Whereas the Hitomi gate valve CalDB file [14][15] was strictly only valid for an on-axis point source, the raytracing results for the XRISM gate valve CalDB file show that it is not restricted to on-axis point sources. An effective transmission probability of unity, and pixel counts ratios of unity are also obtained for a flat, uniform source.

A new CalDB file format and future version of the ARF generator (and xmasim) will allow, in addition, on-the-fly raytracing of the 3-hole gate valve model for arbitrary source spatial distributions and off-axis angles.

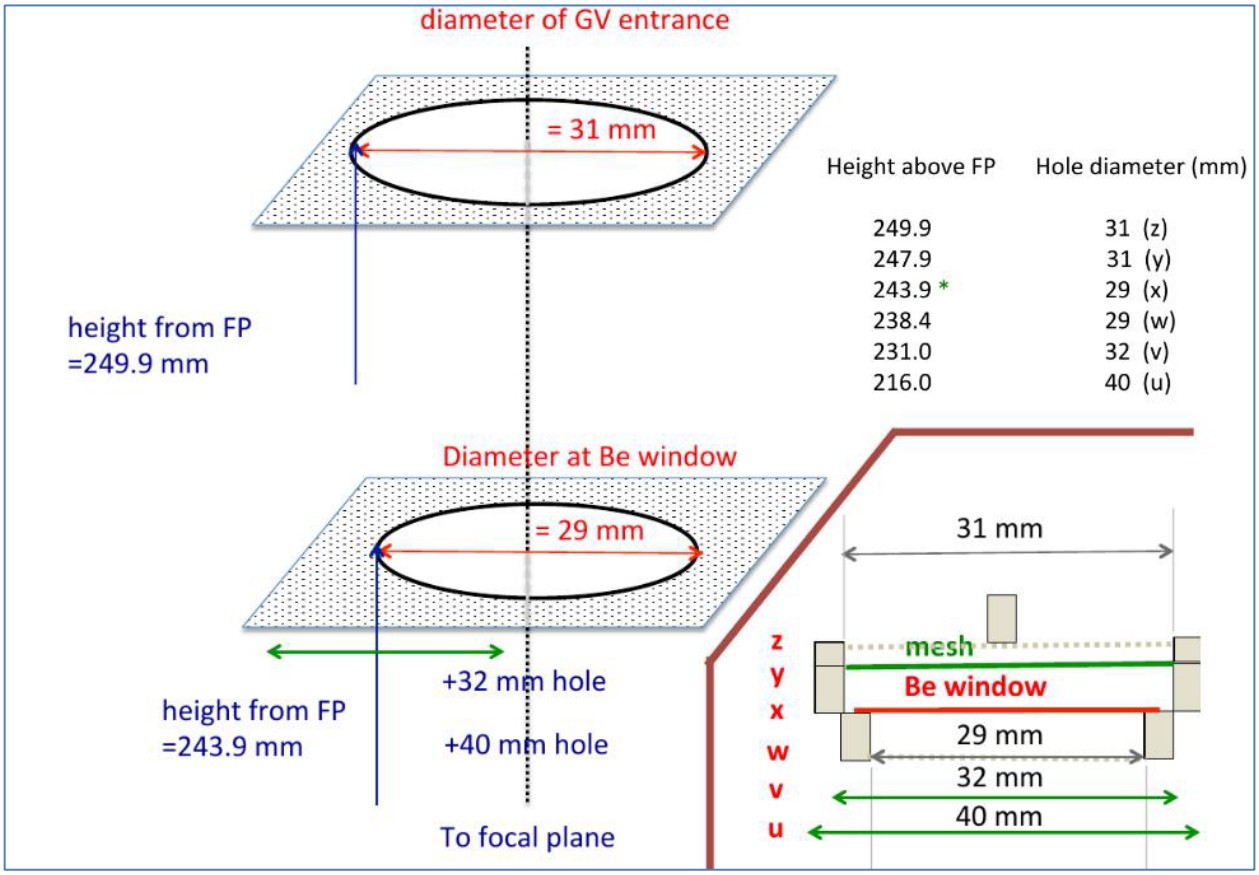

Height above FP	Hole diameter (mm)
249.9	31 (z)
243.9 *	29 (x)
238.4	29 (w)

Figure 16 Top box: components of the Resolve dewar GV taken into account during raytracing [6]. This figure explains the diameter and distance to the focal plane (FP) of each of these features. Bottom box: a simplified "three-hole model" was implemented in the CalDB, which is functionally equivalent to the more complex description.

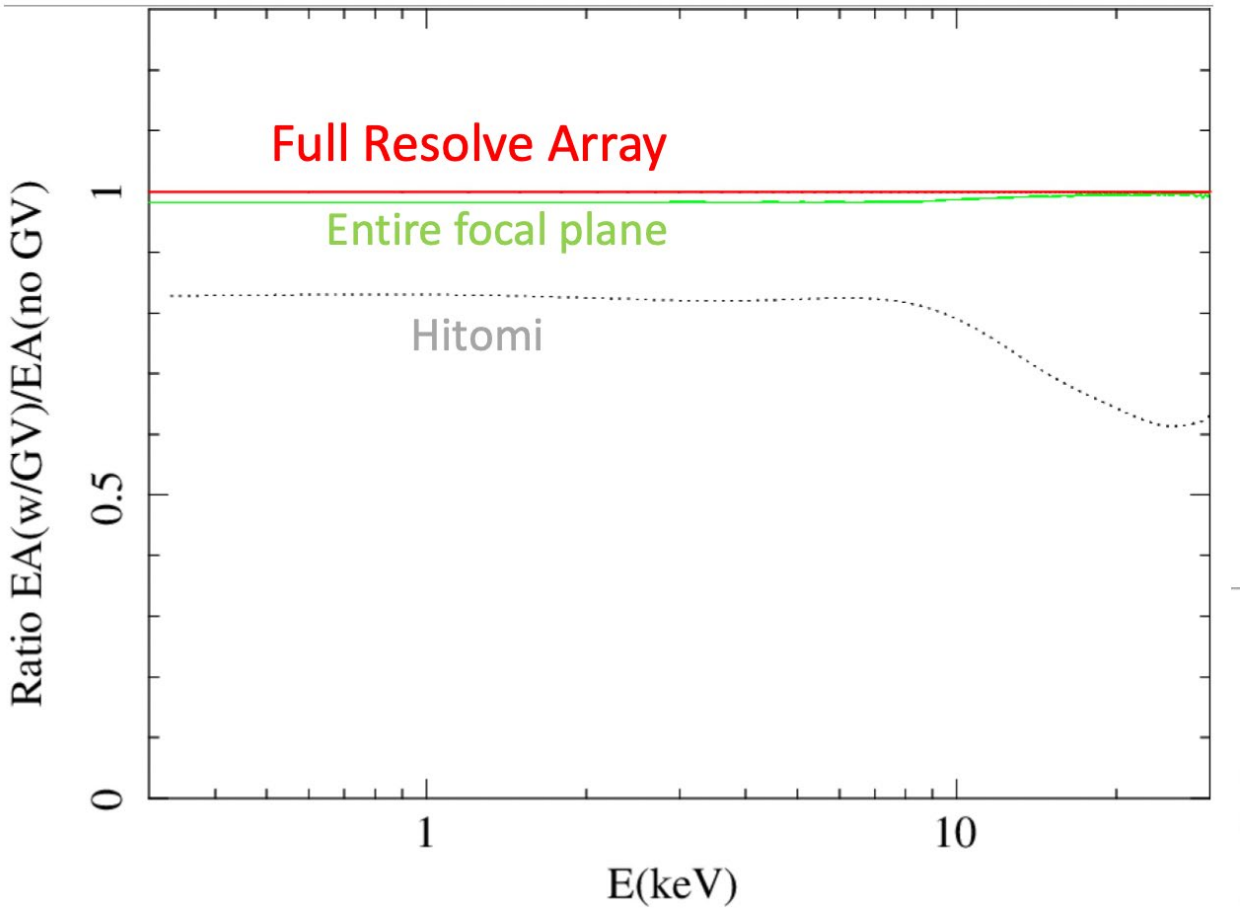

Figure 17 Raytracing results for the 3-hole model and an on-axis point source. The results for the full Resolve array (red curve) remain the same for other test cases including an off-axis point source at 5', a flat uniform source centered on axis, and a flat uniform source centered 5' off axis. In all cases raytracing assumed an OPEN filter with a radius of 43 mm, at a height of 915 mm above the focal plane.

5 References

[1] Midooka, T., 2020, "Ground calibration of XRISM for the initial observations -- X-ray transmission of the gate valve of the cryostat for the low-temperature detector" Master thesis (in Japanese), University of Tokyo
http://www.isas.jaxa.jp/home/ebisawalab/ja/publications/theses/Mthesis_2020_Midooka.pdf
[2] Yoshida, Y. et al., 2017, "Transmission measurement of the spare Beryllium window of the SXS onboard the Hitomi satellite in 2.0-12 keV with KEK-PF", Proc. of SPIE, 103971D
[3] Hoshino, A., et al., 2017, "The evaluation of the Hitomi (Astro-H)/SXS spare beryllium

window in 3.8-30 keV", Proc. of SPIE, 103970E
[4] Tsujimoto, M. et al., 2018, "In-flight calibration of Hitomi Soft X-ray Spectrometer (3) Effective area", PASJ, 70
[5] ICD-0S0120-AR, ASTRO-H SXS (XRISM Resolve) Dewar ICD ver4, SHI, 2019
[6] JAXA-Resolve-ICD-04 "Resolve optical path ICD" ver1.0-draft, 2018
[7] Eckart, M.E. et al. 2016, ASTRO-H Instrument Calibration Report: "SXS gate valve window transmission" ver0.3
[8] https://physics.nist.gov/PhysRefData/Xcom/html/xcom1.html
[9] Hayashi, T., et al., 2015, "Upgrade of the 30 m x-ray pencil beam line at the Institute of Space and Astronautical Science", JATIS, 1, 044004
[10] Authier, A., 2012, "Optical properties of X-rays – dynamical diffraction", Zeitschrift fur Kristallographie, 227, 36
[11] Midooka, T. et al., 2021, "X-ray transmission calibration of the gate valve for the x-ray astronomy satellite XRISM", JATIS, 7, 2, 028005
[12] https://www2.physics.ox.ac.uk/sites/default/files/CrystalStructure_fullnotes6.pdf
[13] M. E. Eckart, et al., "Ground calibration of the Astro-H (Hitomi) soft x-ray spectrometer," JATIS, 4(2), 021406 (2018)
[14] M. E. Eckart, et al., "Instrument Calibration Report, SXS Gate Valve Window Transmission," (2016).
https://heasarc.gsfc.nasa.gov/docs/hitomi/calib/caldb_doc/asth_sxs_caldb_gatevalve_v20161223.pdf
[15] T. Yaqoob, et al., "Instrument Calibration Report, SXS Gate Valve and Filter Wheel Filters," (2016).
https://heasarc.gsfc.nasa.gov/docs/hitomi/calib/caldb_doc/asth_sxs_caldb_filterfiles_v20161223.pdf
[16] B.L. Henke, E.M. Gullikson, and J.C. Davis. *X-ray interactions: photoabsorption, scattering, transmission, and reflection at E=50-30000 eV, Z=1-92*, Atomic Data and Nuclear Data Tables Vol. **54** (no.2), 181-342 (July 1993). http://henke.lbl.gov/optical_constants/asf.html